

# Mn L<sub>2,3</sub> edge resonant scattering in manganites: Influence of the magnetic state

N. Stojić,<sup>1</sup> N. Binggeli,<sup>1,2</sup> and M. Altarelli<sup>1,3</sup>

<sup>1</sup> *Abdus Salam International Centre for Theoretical Physics, Trieste 34014, Italy*

<sup>2</sup> *INFM Democritos National Simulation Center, Trieste I-34014, Italy and*

<sup>3</sup> *Sincrotrone Trieste, Area Science Park, 34012 Basovizza, Trieste, Italy*

(Dated: May 24, 2019)

## Abstract

We present an analysis of the dependence of the resonant orbital order and magnetic scattering spectra on the spin configuration. We consider an arbitrary spin direction with respect to the local crystal field axis, thus lowering significantly the local symmetry. To evaluate the atomic scattering in this case, we generalized the Hannon-Trammel formula and implemented it inside the framework of atomic multiplet calculations in a crystal field. For an illustration, we calculate the magnetic and orbital scattering in the CE phase of La<sub>0.5</sub>Sr<sub>1.5</sub>MnO<sub>4</sub> in the cases when the spins are aligned with the crystal lattice vector  $\vec{a}$  (or equivalently  $\vec{b}$ ) and when they are rotated in the *ab*-plane by 45° with respect to this axis. Magnetic spectra differ for the two cases. For the orbital scattering, we show that for the former configuration there is a non negligible  $\sigma \rightarrow \sigma'$  ( $\pi \rightarrow \pi'$ ) scattering component, which vanishes in the 45° case, while the  $\sigma \rightarrow \pi'$  ( $\pi \rightarrow \sigma'$ ) components are similar in the two cases. From the consideration of two 90° spin canted structures, we conclude there is a significant dependence of the orbital scattering spectra on the spin arrangement. Recent experiments detected a sudden decrease of the orbital scattering intensity upon increasing the temperature above the Néel temperature in La<sub>0.5</sub>Sr<sub>1.5</sub>MnO<sub>4</sub>. We discuss this behavior considering the effect of different types of misorientations of the spins on the orbital scattering spectrum.

PACS numbers: 60.10-i, 71.30.th, 75.25+x, 75.47.Lx

## I. INTRODUCTION

The physics of perovskite-type manganites is one of the very exciting areas of the present-day solid-state research, displaying abundance of interesting phenomena, of which the most known is the huge resistivity change upon the application of magnetic fields, the so-called colossal magnetoresistance effect<sup>1</sup>. Manganites have rich phase diagrams with several types of magnetic, charge and orbitally ordered phases, often exhibiting mesoscale phase coexistence. The physics of these systems is controlled by a complex interplay of magnetic, orbital, charge and structural degrees of freedom. Orbital order is characterized by the spatial arrangement of the outermost valence electrons. Although it was predicted and described theoretically 50 years ago<sup>2</sup>, it has been recognized as a hidden degree of freedom, because of difficulties related to its direct observation.

The resonant x-ray scattering (RXS) is a promising tool for the study of orbital order, and, at the same time, convenient for the study of magnetic and charge ordering. In particular, it can be applied to investigate the correlations between the orbital order parameter and the magnetic and charge order parameters. The first RXS experiments with the goal of detecting orbital ordering were done at the K-edge. At the manganese K-edge, one  $1s$  electron is excited into the empty  $4p$  band after absorption of a photon of the resonant energy. This intermediate state has a finite lifetime, after which the ion emits a photon and relaxes back to the initial state. Today it is believed that the observed signal is not sensitive to the onsite orbital ordering of the  $3d$  orbitals, but to band-structure effects including the effect of the Jahn-Teller crystal field on the  $4p$  states together with the hybridization of the  $4p$  orbitals with the neighboring oxygen orbitals (also controlled by the Jahn-Teller distortion) and with empty  $3d$  orbitals of the neighboring Mn atoms<sup>3,4,5</sup>. Instead, the  $L_{2,3}$ -edge scattering measurements<sup>6,7,8,9,10,11</sup>, stimulated by the theoretical work of Castleton and Altarelli<sup>12</sup>, are sensitive to both the onsite orbital ordering and the Jahn-Teller distortion. At the Mn  $L_{2,3}$  edges, the virtual dipole transition consists of an excitation of one  $2p$  electron into the  $3d$  shell, thus directly probing the orbital ordering. The specific contributions of the orbital ordering and Jahn-Teller distortions must then be disentangled in order to interpret the results of such experiments. This is usually done by comparing the experimental spectra to theoretical simulated spectra. Previous theoretical work<sup>11</sup> has indicated that the Jahn-Teller distortion affects almost exclusively the  $L_3$  edge. However, to monitor the effect of

a change in the magnetic order on the orbital ordering in particular (or on the Jahn-Teller distortion), one needs also to know the direct influence of the magnetic configuration on the orbital spectra. So far, to our knowledge, this effect on the L edge orbital scattering has not been addressed. Also, obviously, if the spin configuration has a significant influence on the orbital scattering, it must be properly included in the analysis used to disentangle the effects of the orbital ordering and Jahn-Teller distortion.

Recently, Wilkins *et al.*<sup>11</sup> reported measurements of the temperature dependence of the orbital scattering at the Mn L<sub>2,3</sub> edge in La<sub>0.5</sub>Sr<sub>1.5</sub>MnO<sub>4</sub> which displayed a substantial decrease in the orbital scattering intensity, as the temperature is raised, at the transition from the antiferromagnetic to paramagnetic phase. Analogous behavior when crossing the Néel temperature was previously reported in LaMnO<sub>3</sub><sup>13</sup>, at the Mn K edge, and in KCuF<sub>3</sub><sup>14,15</sup> at the Cu K edge (but the origin may not be the same). More recently, Staub *et al.*<sup>9</sup> also presented measurements of the temperature dependence of the orbital scattering at the Mn L<sub>2,3</sub> edge in La<sub>0.5</sub>Sr<sub>1.5</sub>MnO<sub>4</sub>, which showed a smaller change at the Néel temperature. Furthermore, based on a polarization analysis, they showed that the orbital signal below the Néel temperature includes a non negligible contribution of magnetic scattering from twinned minority ferromagnetic domains. However, it is still unclear whether this fully explains the temperature dependence of the observed orbital signal<sup>9,11</sup>. In principle, the change in the magnetic configuration at the Néel temperature could also affect the spectrum.

In this work we address the direct influence of the magnetic configuration on the orbital scattering spectra. As a prototype system, we focus on La<sub>0.5</sub>Sr<sub>1.5</sub>MnO<sub>4</sub>. We find that the spin configuration has indeed an influence on the orbital scattering, but mostly when the spins are noncollinear. For the magnetic scattering we find that the spin configuration has a significant influence on the spectrum, and this even in the collinear CE structure. Previous studies generally considered spin oriented along the highest local symmetry axis of the Mn<sup>3+</sup> crystallographic site. In order to allow an arbitrary orientation of the spin with respect to the local crystal field axis, we generalized the Hannon-Trammell formula<sup>16</sup> for atomic scattering, derived for spherical local site symmetry, by a systematic expansion in invariants of decreasing symmetry down to C<sub>i</sub>. We use these results to derive the scattering formulae for different spin configurations, including the polarization dependence. Finally, we consider various types of spin misalignments and misorientations to understand the effect of spin disorder on the orbital spectrum of the paramagnetic phase. We separately discuss

the effect of the loss of spin order between the *ab*-planes at temperatures just above  $T_N$  and spin misalignments inside these planes at higher temperatures.

This work is organized as follows: in Section II we describe the system and the theoretical method, while in Section III we present the scattering formula in the  $C_i$  symmetry, and its applications towards the description of the orbital and magnetic scattering in four special cases of spin arrangement. In Section IV, we present the corresponding orbital and magnetic spectra for  $\text{La}_{0.5}\text{Sr}_{1.5}\text{MnO}_4$  and address the influence of the spin configuration, while in Section V we discuss our results in connection with the issue of the orbital spectrum of the paramagnetic phase. Section VI gives the conclusions of the work, while two appendices describe some calculational details.

## II. DESCRIPTION OF THE SYSTEM AND THEORETICAL APPROACH

In the present work, we focus our attention on the half doped manganites with a low temperature CE antiferromagnetic structure. As an example, we consider the  $\text{La}_{0.5}\text{Sr}_{1.5}\text{MnO}_4$  compound, which displays a variety of phases<sup>17,18</sup>. The charge and orbitally ordered phase sets on upon cooling at 230 K. The disproportionation of the Mn ions into the formal valences  $\text{Mn}^{3+}$  and  $\text{Mn}^{4+}$  is usually assumed, while recent experiments<sup>19</sup> indicate that the charge difference in manganite materials is much smaller than 1. In the present atomic-based approach, we approximate the charge on the manganese ions by the integral values of 3+ and 4+. The four (five) 3d electrons of the  $\text{Mn}^{3+}$  (the  $\text{Mn}^{4+}$ ) are under the strong influence of the crystal field. In the presence of the cubic ligand field, the degenerate *d* orbitals split into triple degenerate  $t_{2g}$  and doubly degenerate  $e_g$  levels. Cooperative Jahn-Teller distortions of the  $\text{MnO}_6$  octahedra further reduce the symmetry of the crystal field to  $D_{4h}$  and thus lift the orbital degeneracy.  $t_{2g}$  level splits into  $d_{xy}$  and doubly-degenerate  $d_{xz,yz}$  orbitals, and  $e_g$  into orbitals of the  $d_{3z^2-r^2}$  and  $d_{x^2-y^2}$  type. Only one of the  $e_g$  orbitals is occupied on the  $\text{Mn}^{3+}$  ions, leading to orbital ordering, *i.e.* an alternate arrangement of orbitals oriented along the  $\vec{a}$  and  $\vec{b}$  axes on neighboring  $\text{Mn}^{3+}$  A and B sites (see Fig. 1). The antiferromagnetic phase, characterized as the CE type structure, exists under 115 K. In this phase, the spins are lying in the *ab*-plane<sup>20</sup>, displaying ferromagnetic ordering along spin-chains in the *ab*-plane (see Fig. 1:  $\text{A}^- - \text{B}^- - \text{A}^-$  and  $\text{A}^+ - \text{B}^+ - \text{A}^+$  spin chains, “+” and “-” refer to the spin direction) and antiferromagnetic ordering between

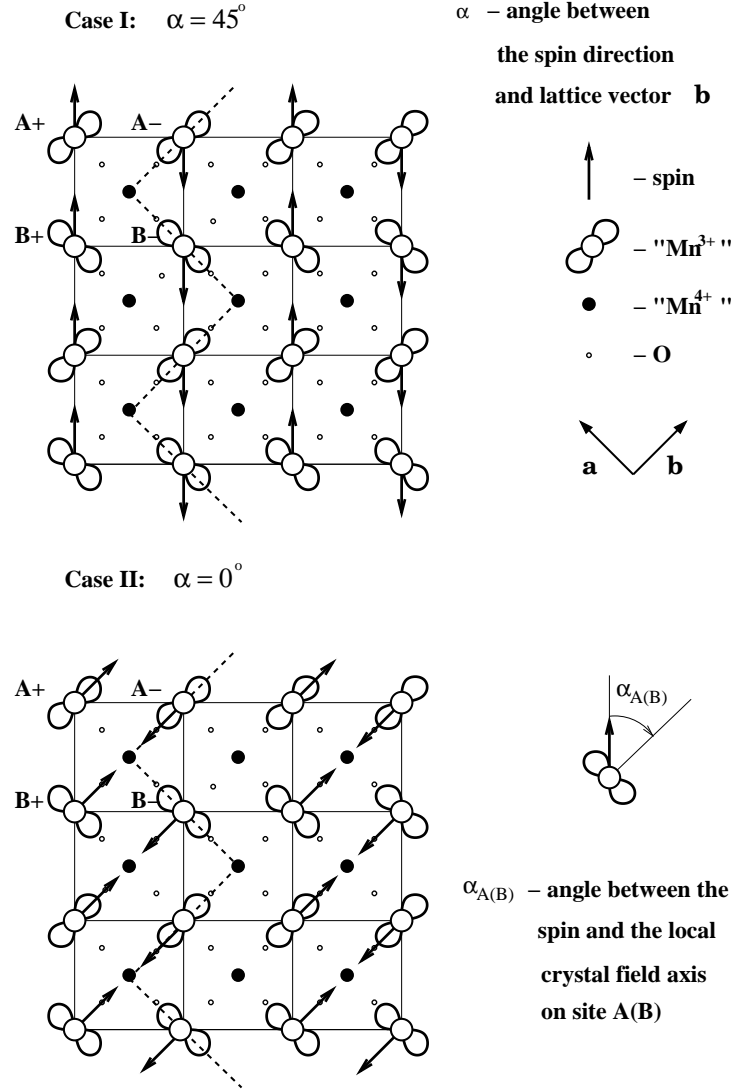


FIG. 1: The  $\text{MnO}_2$  plane of  $\text{La}_{0.5}\text{Sr}_{1.5}\text{MnO}_4$  representing charge, orbital and spin ordering for two different cases of spin orientation in the CE structure. Case I: the spin and crystal axis  $\vec{b}$  enclose an angle  $\alpha = 45^\circ$  and Case II:  $\alpha = 0^\circ$ . The dashed lines denote the ferromagnetic spin chains. For reasons of clarity, the spins on the “ $\text{Mn}^{4+}$ ” ions are omitted. We assumed the  $x^2 - y^2/z^2 - y^2$  type of orbital ordering<sup>11</sup>.

the spin chains both in the  $ab$ -plane and along the  $c$ -axis.

Figure 1 presents two possible cases of spin orientation in the CE structure, which we will consider in the present work. In Case I, the spins are parallel to the  $\vec{a} + \vec{b}$  axis, corresponding to an angle  $\alpha = 45^\circ$  between the spin direction and the crystal  $\vec{b}$  axis. In Case II, instead,

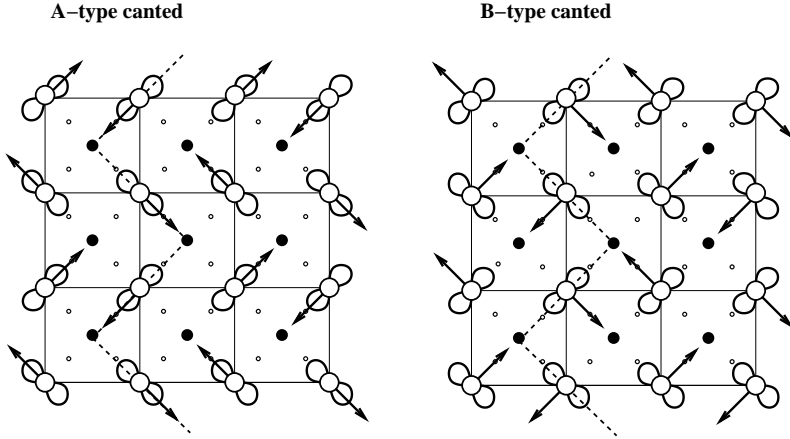


FIG. 2: The  $\text{MnO}_2$  plane of  $\text{La}_{0.5}\text{Sr}_{1.5}\text{MnO}_4$  representing charge, orbital and spin ordering for two hypothetical  $90^\circ$ -spin-canted structures.

the spins are parallel to the  $\vec{b}$  axis ( $\alpha = 0^\circ$ ).

Having in mind the paramagnetic phase and the effect of spin misorientations on the orbital spectrum, we will also consider two  $90^\circ$ -spin-canted structures, which are illustrated in Fig. 2. These structures, “A-type canted” and “B-type canted”, are built using local atomic configurations of Case II in Fig 1. The A-type canted is obtained using the  $\text{Mn}^{3+}$   $\text{A}^{(+,-)}$  configurations (spin parallel to the orbital) and the B-type canted using the  $\text{Mn}^{3+}$   $\text{B}^{(+,-)}$  configurations (spin perpendicular to the orbital), with possible  $90^\circ$  rotations of these atomic building blocks. We note that, for the orbital scattering, only  $\text{Mn}^{3+}$  sites need to be considered. Also, for the magnetic scattering of the CE structures, we will consider (as in the experiments<sup>10,11</sup>) only superlattice reflections which selectively probe the  $\text{Mn}^{3+}$  spins contribution.

We based our calculations of the RXS spectra on atomic multiplet formulation in a crystal field<sup>21,22</sup>. Cowan’s atomic multiplet program<sup>23,24</sup> provides the Hartree-Fock values of the radial Coulomb (Slater) integrals  $F^{0,2,4}(d, d)$ ,  $F^2(p, d)$ ,  $G^{1,3}(p, d)$  (direct and exchange contributions) and the spin-orbit interactions  $\zeta(2p)$  and  $\zeta(3d)$  for an isolated  $\text{Mn}^{3+}$  ion at 0 K. They are given in Table I. It is known that the strengths of the Coulomb integrals in a solid are reduced due to the screening effects to about  $\sim 70\text{-}80\%$  of the atomic values<sup>25</sup>. The largest of these integrals are nearly an order of magnitude greater than the crystal field splittings. This fact justifies our choice of the atomic multiplet approach in a crystal field.

	$F^2(d, d)$	$F^4(d, d)$	$F^2(p, d)$	$G^1(p, d)$	$G^3(p, d)$	$\zeta(2p)$	$\zeta(3d)$
$3d^4$	11.415	7.148	—	—	—	—	0.046
$2p^53d^5$	12.210	7.649	6.988	5.179	2.945	7.467	0.059

TABLE I: The Hartree-Fock values for the ground and excited states of  $\text{Mn}^{3+}$  given in eV. The  $p$ -shell spin-orbit parameter  $\zeta(2p)$  has been increased by 9 % from the Hartree-Fock value to correspond to the experimental value<sup>26</sup>.

The treatment of the crystal field in this model is based on symmetry considerations. Starting from the transition matrix elements evaluated in the spherical point group, we lower the symmetry by the inclusion of a crystal field, following a “branching” of point groups. For example, the following “branching” can be generated:  $O_3 \supset O_h \supset D_{4h} \supset D_{2h} \supset C_i$ <sup>27</sup>. For the calculation of the matrix elements in a given point group, the Wigner-Eckart theorem is used. In practice, this theorem is applied through a multiplication of the matrix element evaluated in the  $O_3$  point group by a chain of 2-j and 3-j coefficients for each branching. This is implemented in a crystal field code, which gives the energy spectrum and the dipole transition matrix elements necessary for the calculation of the scattering spectra. The values of the cubic ( $X^{400}$ ) and tetragonal ( $X^{220}$ ) crystal field parameters are obtained from a fit to the experimental RXS spectra. In the present case, we will use the values obtained in Ref. 11 for  $\text{La}_{0.5}\text{Sr}_{1.5}\text{MnO}_4$ . These values are  $X^{400} = 5.6$  eV and  $X^{220} = 3.75$  eV, and correspond to an  $x^2 - y^2/y^2 - z^2$  type of orbital ordering (with the x, y, and z axes along  $\vec{a}$ ,  $\vec{b}$  and  $\vec{c}$ , respectively). All the Slater integrals were scaled down to 75 % of their atomic values<sup>25,28</sup>. Furthermore, in order to simulate the effects of the spin ordering on an isolated ion (superexchange and direct exchange interactions), we introduce a magnetic field acting on the spin of the atom. This field splits additionally the  $S = 2$  quintet into  $S_z = -2, -1, \dots, 2$  levels. Inclusion of the magnetic field favors the  $S_z = -2$  level as the ground state of the atom. The value of the Zeeman energy is set to 0.02 eV.

### III. SCATTERING FORMULA

In the first part of this section we describe atomic scattering for a general orientation of the spin axes with respect to the local crystal field axes. Thereafter, we apply the atomic

scattering formula to find expressions for the orbital scattering of the four different spin structures considered and the magnetic scattering for the two different orientations of the spins in the antiferromagnetic CE-phase.

### A. Systematic expansion of the atomic scattering amplitude in invariants of decreasing symmetry

To calculate a diffraction spectrum, we first evaluate the atomic scattering from a single site and then add up the contributions of the atoms in the whole crystal. The type of order is selected by the scattering vector  $\vec{q}$  which describes the periodicity of the orbital, magnetic or charge order. Depending on the relative orientation of the local crystal field axis and the spin direction, the local symmetry can change. In the case in which the crystal and spin axes are collinear, the site symmetry corresponds to the one of the crystal field. We use a tetragonal crystal field<sup>29</sup>, described by the  $D_{4h}$  point group. If the spin direction, however, differs from the crystal field axis, the local symmetry can be as low as that of the  $C_i$  point group.

Following the approach by Carra and Thole<sup>30</sup>, we write the scattering amplitude as a linear combination of the product of pairs of tensors of increasing rank, which transform according to the irreducible representations of the spherical group  $SO_3$ . To lower the symmetry to the  $C_i$  point group, we need to branch each irreducible representation into subgroup of irreducible representations, following the chain:  $O_3 \supset O_h \supset D_{4h} \supset C_{4h} \supset C_{2h} \supset C_i$ . Only the totally symmetric representations contribute to the atomic scattering amplitude. If we stop the branching at the  $C_{4h}$  point group, we find for the atomic scattering amplitude the following expression:

$$F_{\text{res}, C_{4h}}^{E_1} = \frac{3}{4} \lambda \left\{ (\hat{\mathbf{e}}_f^* \cdot \hat{\mathbf{e}}_i) (F_{1;1} + F_{-1;-1}) - i \left[ (\hat{\mathbf{e}}_f^* \times \hat{\mathbf{e}}_i) \cdot \hat{\mathbf{z}} \right] (F_{1;1} - F_{-1;-1}) + (\hat{\mathbf{e}}_f^* \cdot \hat{\mathbf{z}}) (\hat{\mathbf{e}}_i \cdot \hat{\mathbf{z}}) (2F_{0;0} - F_{1;1} - F_{-1;-1}) \right\}, \quad (1)$$

where  $\lambda$  represents a scattering coefficient<sup>30</sup>,  $\hat{\mathbf{e}}_i(\hat{\mathbf{e}}_f)$  is the incoming (outgoing) photon polarization, and  $F_{m;m'}$  is defined as:

$$F_{m;m'} = \sum_n \frac{\langle 0 | J_m^{1\dagger} | n \rangle \langle n | J_{m'}^1 | 0 \rangle}{E_0 - E_n + \hbar\omega + i\Gamma/2}, \quad (2)$$

where  $m$  and  $m'$  denote polarization states and  $J_m^1$  are the electric dipole operators defined in spherical coordinates.  $|0\rangle$  represents the ground state with energy  $E_0$  and  $|n\rangle$  an intermediate

state with energy  $E_n$ . The photon energy is  $\hbar\omega$  and  $\Gamma$  represents the broadening due to the core-hole lifetime. The local coordinate system is chosen in such a way that the z-axis corresponds to the highest local symmetry axis, which is also the quantization (spin) direction. The same result is known as the Hannon-Trammel formula<sup>16</sup>, which was derived for the spherical symmetry, and is applicable up to local symmetries as low as that of the  $C_{4h}$  point group. Lowering the symmetry to the  $C_{2h}$  point group, the following expression for the atomic scattering amplitude is found:

$$f_{\text{res}, C_{2h}}^{E_1} = f_{\text{res}, C_{4h}}^{E_1} + \frac{3}{4}\lambda \left\{ \left[ (\hat{\mathbf{e}}_f^* \cdot \hat{\mathbf{y}})(\hat{\mathbf{e}}_i \cdot \hat{\mathbf{y}}) - (\hat{\mathbf{e}}_f^* \cdot \hat{\mathbf{x}})(\hat{\mathbf{e}}_i \cdot \hat{\mathbf{x}}) \right] (F_{-1;1} + F_{1;-1}) + \right. \\ \left. i \left[ (\hat{\mathbf{e}}_f^* \cdot \hat{\mathbf{x}})(\hat{\mathbf{e}}_i \cdot \hat{\mathbf{y}}) + (\hat{\mathbf{e}}_f^* \cdot \hat{\mathbf{y}})(\hat{\mathbf{e}}_i \cdot \hat{\mathbf{x}}) \right] (F_{-1;1} - F_{1;-1}) \right\}, \quad (3)$$

where  $\hat{\mathbf{x}}$ ,  $\hat{\mathbf{y}}$ , and  $\hat{\mathbf{z}}$  are unit vectors corresponding to a right Cartesian coordinate system, with the z-axis defined as above. Finally, assuming no symmetry operation on the site, except the inversion, we obtain four additional terms in the description of the atomic scattering amplitude in the  $C_i$  point group:

$$f_{\text{res}, C_i}^{E_1} = f_{\text{res}, C_{2h}}^{E_1} + \frac{3}{4}\lambda \left\{ -i \frac{\sqrt{2}}{2} \left[ (\hat{\mathbf{e}}_f^* \cdot \hat{\mathbf{y}})(\hat{\mathbf{e}}_i \cdot \hat{\mathbf{z}}) - (\hat{\mathbf{e}}_f^* \cdot \hat{\mathbf{z}})(\hat{\mathbf{e}}_i \cdot \hat{\mathbf{y}}) \right] (F_{1;0} + F_{-1;0} + F_{0;1} + F_{0;-1}) + \right. \\ \frac{\sqrt{2}}{2} \left[ (\hat{\mathbf{e}}_f^* \cdot \hat{\mathbf{x}})(\hat{\mathbf{e}}_i \cdot \hat{\mathbf{z}}) - (\hat{\mathbf{e}}_f^* \cdot \hat{\mathbf{z}})(\hat{\mathbf{e}}_i \cdot \hat{\mathbf{x}}) \right] (-F_{1;0} - F_{0;-1} + F_{-1;0} + F_{0;1}) + \\ -i \frac{\sqrt{2}}{2} \left[ (\hat{\mathbf{e}}_f^* \cdot \hat{\mathbf{y}})(\hat{\mathbf{e}}_i \cdot \hat{\mathbf{z}}) + (\hat{\mathbf{e}}_f^* \cdot \hat{\mathbf{z}})(\hat{\mathbf{e}}_i \cdot \hat{\mathbf{y}}) \right] (F_{1;0} + F_{-1;0} - F_{0;1} - F_{0;-1}) + \\ \left. \frac{\sqrt{2}}{2} \left[ (\hat{\mathbf{e}}_f^* \cdot \hat{\mathbf{x}})(\hat{\mathbf{e}}_i \cdot \hat{\mathbf{z}}) + (\hat{\mathbf{e}}_f^* \cdot \hat{\mathbf{z}})(\hat{\mathbf{e}}_i \cdot \hat{\mathbf{x}}) \right] (-F_{1;0} + F_{0;-1} + F_{-1;0} - F_{0;1}) \right\}, \quad (4)$$

where x, y, and z are unit vectors of any right Cartesian coordinate system, but it is convenient to choose, also in this case, the z-axis along the spin direction.

## B. Orbital order scattering

In tetragonal CE structures, the wave vectors probing the antiferro orbital ordering are:  $\vec{q}^{\text{OO}} = (\frac{1+2n}{4} - \frac{m}{2}, \frac{1+2n}{4} + \frac{m}{2}, l)$  in units of  $(\frac{2\pi}{a}, \frac{2\pi}{a}, \frac{2\pi}{c})$ , where  $n$ ,  $m$ , and  $l$  are integers and  $a$ ,  $c$  are the lattice constants. Taking into account the structure factors, the scattering amplitude for orbital wave vectors is proportional to the following combination of the atomic scattering amplitudes at the A<sup>(+,-)</sup> and B<sup>(+,-)</sup> sites:  $f^{A+} + f^{A-} - f^{B+} - f^{B-}$ . In the soft x-ray experiments<sup>7,9,10</sup> the orbital order wave vector was taken as  $\vec{q}^{\text{OO}} = (\frac{1}{4}, \frac{1}{4}, 0)$ , and this is the wave vector we will consider for the polarization analysis presented in the next parts of this section. The equations will be presented using as reference system for the components of

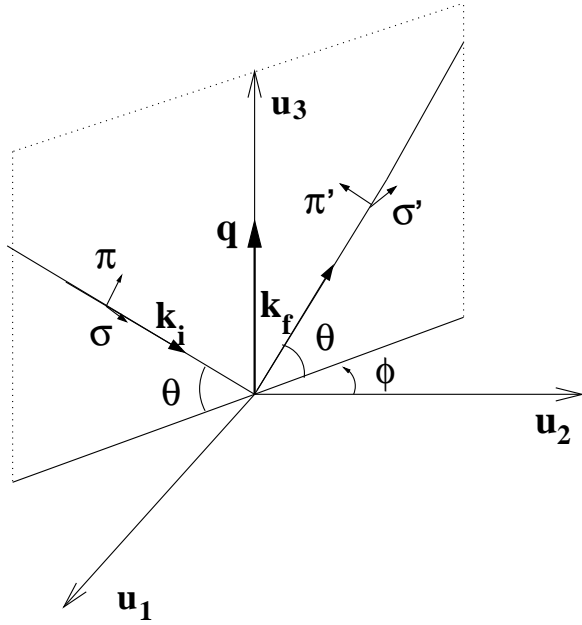


FIG. 3: The scattering plane with the definition of the scattering and azimuthal angles  $\theta$  and  $\phi$ .  $\vec{k}_i$  ( $\vec{k}_f$ ) is the incident (outcoming) photon wavevector,  $\vec{q} = \vec{k}_f - \vec{k}_i$ . For the case of orbital order scattering with  $\vec{q}^{OO} = (\frac{1}{4}, \frac{1}{4}, 0)$ , the reference axes are:  $\vec{u}_1 = \frac{1}{\sqrt{2}}[\bar{1}10]$ ,  $\vec{u}_2 = [001]$  and  $\vec{u}_3 = \frac{1}{\sqrt{2}}[110]$  in the crystal coordinate system  $\vec{a}$ ,  $\vec{b}$ ,  $\vec{c}$ . For the magnetic scattering,  $\vec{q}^{AF} = (\frac{1}{4}, -\frac{1}{4}, \frac{1}{2})$  and the following reference axes are used:  $\vec{u}_1 = \frac{1}{\sqrt{3}}[1\bar{1}\bar{1}]$ ,  $\vec{u}_2 = \frac{1}{\sqrt{2}}[110]$  and  $\vec{u}_3 = \frac{1}{\sqrt{6}}[1\bar{1}2]$ .

the atomic scattering tensors  $F_{m,m'}$  the local coordinate system in which the z-axis remains in the spin direction, x lies in the  $ab$ -plane and the y-axis is perpendicular to the  $ab$ -plane.

### 1. Case I: $\alpha = 45^\circ$

For the case when  $\alpha = 45^\circ$ , it is useful to note that starting from the configuration at site A+, in Fig. 1, and using symmetry operations (rotation by  $180^\circ$  about the  $\vec{c}$  or  $(\vec{a} + \vec{b})$  axis) one can obtain the configurations at the remaining three sites. This simplifies the numerical part of the calculation, because it suffices to perform an atomic calculation for just one site. The local symmetry of each site is described by the  $C_i$  point group. From inspection of Eq. 4 it can be seen that the only nonvanishing terms of the orbital order scattering are the ones including  $(\hat{\mathbf{e}}_f^* \cdot \hat{\mathbf{x}})(\hat{\mathbf{e}}_i \cdot \hat{\mathbf{z}})$  and  $(\hat{\mathbf{e}}_f^* \cdot \hat{\mathbf{z}})(\hat{\mathbf{e}}_i \cdot \hat{\mathbf{x}})$  polarization factors. Furthermore, the very last term from Eq. 4 vanishes, in our case, as the matrix elements from Eq. 2 are real.<sup>31</sup> After evaluation of the polarization factor we obtain the following expression for the orbital order

scattering intensity:

$$f_{\text{res}}^{\text{OO}} = \cos \theta \cos \phi \left( -F_{1;0}^{A+} + F_{0;-1}^{A+} + F_{-1;0}^{A+} - F_{0;1}^{A+} \right), \quad (5)$$

in the case of  $\sigma \rightarrow \pi'$  or  $\pi \rightarrow \sigma'$  polarization. In Eq. 5 the scattering and azimuthal angles  $\theta$  and  $\phi$  are defined as shown in Fig. 3, using as reference axes  $\vec{u}_1 = \frac{1}{\sqrt{2}}[\bar{1}10]$ ,  $\vec{u}_2 = [001]$  and  $\vec{u}_3 = \frac{1}{\sqrt{2}}[110]$ . The scattering amplitude vanishes in the case of  $\sigma \rightarrow \sigma'$  or  $\pi \rightarrow \pi'$  polarization. The F-part of Eq. 5 can be written in Cartesian coordinates as  $2F_{xz}$ .

## 2. Case II: $\alpha = 0^\circ$

In the case when the angle  $\alpha$  is different from  $45^\circ$ , the sites A and B are inequivalent, since the spin encloses two different angles,  $\alpha_A$  and  $\alpha_B$ , with the local crystal field axis at sites A and B. Case II, with  $\alpha = 0^\circ$  in Fig. 1, illustrates the situation with the highest local site symmetry, when the spin is collinear with the crystal field axis at site B ( $\alpha_B = 0^\circ$ ), and perpendicular to the local crystal field axis at site A ( $\alpha_A = 90^\circ$ ). The local site symmetries for the B and A sites are  $C_{4h}$  and  $C_{2h}$  respectively. For the evaluation of orbital scattering, we add the contributions from the four sites in the same manner as we did in the previous case, because the orbital ordering remains unchanged. But, this time, we need to do atomic calculations for two different sites, as there is no symmetry operation relating sites A and B. For the same reason, there will be no cancellation of contributions from various terms, which we had previously, and the expression describing orbital order scattering amplitude will have the following form for  $\sigma$  polarized incident light:

$$f_{\text{res}}^{\text{OO},\sigma_{\text{inc}}} = \left\{ \begin{array}{l} \frac{1}{2} \cos^2 \phi \\ \frac{1}{2} \cos \phi (\sin \theta \sin \phi - \cos \theta) \\ \sin^2 \phi + \frac{1}{2} \cos^2 \phi \\ \frac{1}{2} \cos \theta \cos \phi \end{array} \right\} [2(F_{0;0}^{A+} - F_{0;0}^{B+})] + \left\{ \begin{array}{l} \frac{1}{2} \cos^2 \phi - \sin^2 \phi \\ \frac{1}{2} \cos \phi (3 \sin \theta \sin \phi + \cos \theta) \end{array} \right\} [F_{-1;-1}^{A+} + F_{1;1}^{A+} - (F_{-1;-1}^{B+} + F_{1;1}^{B+})] + \left\{ \begin{array}{l} \frac{1}{2} \cos^2 \phi + F_{-1;1}^{A+} + F_{1;-1}^{A+} - (F_{-1;1}^{B+} + F_{1;-1}^{B+}) \end{array} \right\}, \quad (6)$$

where the upper expression in the curly brackets represents the  $\sigma \rightarrow \sigma'$  polarization part and the bottom one the  $\sigma \rightarrow \pi'$  contribution. The superscripts A and B denote the two different sites. The second term on the right hand side of Eq. 6 is proportional to  $F_{xx} + F_{yy}$  in the Cartesian coordinates and the third one to  $F_{xx} - F_{yy}$ . The angles  $\theta$  and  $\phi$  are defined

in Fig 3. To simplify the polarization factors, we evaluate the polarization dependence for the azimuthal angle, using the value  $\phi = 0^\circ$ , as in the experiment (Ref. 10). Taking this into account, Eq. 6 can be rewritten in a simpler form and in the Cartesian coordinates:

$$f_{\text{res}}^{\text{OO},\sigma\text{inc}} = \begin{Bmatrix} 1 \\ 0 \end{Bmatrix} \left[ F_{xx}^{A+} + F_{zz}^{A+} - (F_{xx}^{B+} + F_{zz}^{B+}) \right] + \begin{Bmatrix} 0 \\ \cos \theta \end{Bmatrix} \left[ F_{xx}^{A+} - F_{zz}^{A+} - (F_{xx}^{B+} - F_{zz}^{B+}) \right]. \quad (7)$$

We note the important fact that in the  $\alpha = 0^\circ$  case, the  $\sigma \rightarrow \sigma'$  polarization factor is nonvanishing, in contrast to the  $\alpha = 45^\circ$  case.

In the case of  $\pi$  incident polarization, the scattering amplitude reads:

$$f_{\text{res}}^{\text{OO},\pi\text{inc}} = \begin{Bmatrix} \frac{1}{2}(\cos^2 \theta - \sin^2 \theta \sin^2 \phi) \\ -\frac{1}{2} \cos \phi (\sin \theta \sin \phi + \cos \theta) \end{Bmatrix} \left[ 2(F_{0;0}^{A+} - F_{0;0}^{B+}) \right] + \begin{Bmatrix} \frac{1}{2} \cos^2 \theta - \sin^2 \theta (\cos^2 \phi + \frac{1}{2} \sin^2 \phi) \\ \frac{1}{2} \cos \phi (\cos \theta + \sin \theta \sin \phi) \end{Bmatrix} \left[ F_{-1;-1}^{A+} + F_{1;1}^{A+} - (F_{-1;-1}^{B+} + F_{1;1}^{B+}) \right] + \begin{Bmatrix} \frac{1}{2} \cos^2 \theta + \sin^2 \theta (\cos^2 \phi - \frac{1}{2} \sin^2 \phi) \\ \frac{1}{2} \cos \phi (-3 \sin \theta \sin \phi + \cos \theta) \end{Bmatrix} \left[ F_{-1;1}^{A+} + F_{1;-1}^{A+} - (F_{-1;1}^{B+} + F_{1;-1}^{B+}) \right], \quad (8)$$

where the upper (lower) expression in the curly brackets corresponds to the  $\pi \rightarrow \pi'$  ( $\pi \rightarrow \sigma'$ ) polarization channel. Considering again  $\phi = 0^\circ$ , we see that all three terms on the right hand side of Eq. 8 contribute to the  $\pi \rightarrow \pi'$  scattering, while the expression for the  $\pi \rightarrow \sigma'$  scattering is the same as in the case of the  $\sigma$ -polarized incident light.

### 3. Canted structures

The orbital scattering amplitude for the two canted structures in Fig. 2 can be described by the following expression in the Cartesian coordinates:

$$f_{\text{res}}^{\text{OO},\sigma\text{inc}} = \begin{Bmatrix} 0 \\ \cos \theta \end{Bmatrix} \left[ F_{xx}^{A+} - F_{zz}^{A+} - (F_{xx}^{B+} - F_{zz}^{B+}) \right], \quad (9)$$

assuming as above  $\phi = 0^\circ$ , and using the same convention as in Eqs. 6 and 7 for the polarization channels. For incident  $\sigma$  polarization, the scattering takes place exclusively in the  $\sigma \rightarrow \pi'$  channel.

### C. Magnetic scattering

We performed a similar analysis for the magnetic scattering of the antiferromagnetic CE structures, considering the wave vector  $\vec{q}^{AF} = (\frac{1}{4}, -\frac{1}{4}, \frac{1}{2})$  which probes the antiferromagnetic order of the Mn<sup>3+</sup> atoms and was used in the experiment (Ref. 10). The corresponding magnetic scattering amplitude is proportional to:  $f_{AF} = f^{A+} + f^{B+} - f^{A-} - f^{B-}$ . In the case  $\alpha = 45^\circ$  the only contributing term from Eq. 4 is the second term, and, therefore, the antiferromagnetic scattering amplitude for incident  $\sigma$ -polarized light can be calculated from the expression:

$$f_{\text{res}}^{\text{AF},\sigma\text{inc}} = -\cos\theta \sin\phi (F_{1;1}^{A+} - F_{-1;-1}^{A+}), \quad (10)$$

and in the case  $\alpha = 0^\circ$ :

$$f_{\text{res}}^{\text{AF},\sigma\text{inc}} = \left[ \cos\theta \left( \frac{\sqrt{2}}{2} \sin\phi - \frac{\sqrt{3}}{3} \cos\phi \right) + \frac{\sqrt{6}}{6} \sin\theta \right] (F_{1;1}^{A+} - F_{-1;-1}^{A+} + F_{1;1}^{B+} - F_{-1;-1}^{B+}). \quad (11)$$

The angles  $\theta$  and  $\phi$  have been defined as shown in Fig. 3, with the following definitions of the reference axes:  $\vec{u}_1 = \frac{1}{\sqrt{3}}[1\bar{1}\bar{1}]$ ,  $\vec{u}_2 = \frac{1}{\sqrt{2}}[110]$  and  $\vec{u}_3 = \frac{1}{\sqrt{6}}[1\bar{1}2]$ . There is no  $\sigma \rightarrow \sigma'$  contribution and the polarization factor in Eqs. 10 and 11 is evaluated for the  $\sigma \rightarrow \pi'$  polarization. In the Cartesian coordinates, the F-factor from Eq. 10 and 11 can be expressed as  $F_{xy} - F_{yx}$ .

## IV. INFLUENCE OF THE SPIN ORIENTATION ON THE SCATTERING SPECTRA

In Fig. 4, we compare the calculated orbital order spectra of the CE structures with the two different spin orientations,  $\alpha = 0^\circ$  and  $\alpha = 45^\circ$ , displayed in Fig. 1. We present the spectra for  $\sigma$  and  $\pi$  incident polarization evaluated using the equations derived in the previous section. In the case of the  $\sigma$  incident polarization, panel a) displays the spectrum for the  $\sigma \rightarrow \sigma'$  polarization, panel b) for the  $\sigma \rightarrow \pi'$  polarization, while the simulated experimental situation without a polarization analyzer for the outcoming photons is presented in panel c). Similarly, for the  $\pi$  incident polarization, we present the  $\pi \rightarrow \pi'$  scattering channel on panel a),  $\pi \rightarrow \sigma'$  on panel b) and the average of the two in panel c). The polarization dependence was calculated for the actual experimental angles:  $\theta = 62.9^\circ$  and  $\phi = 0^\circ$ <sup>10</sup>. We used  $\Gamma = 0.5$  eV for the broadening due to the core-hole lifetime and the scattering intensity was convoluted with a Gaussian of width 0.1 eV to simulate the experimental (energy)

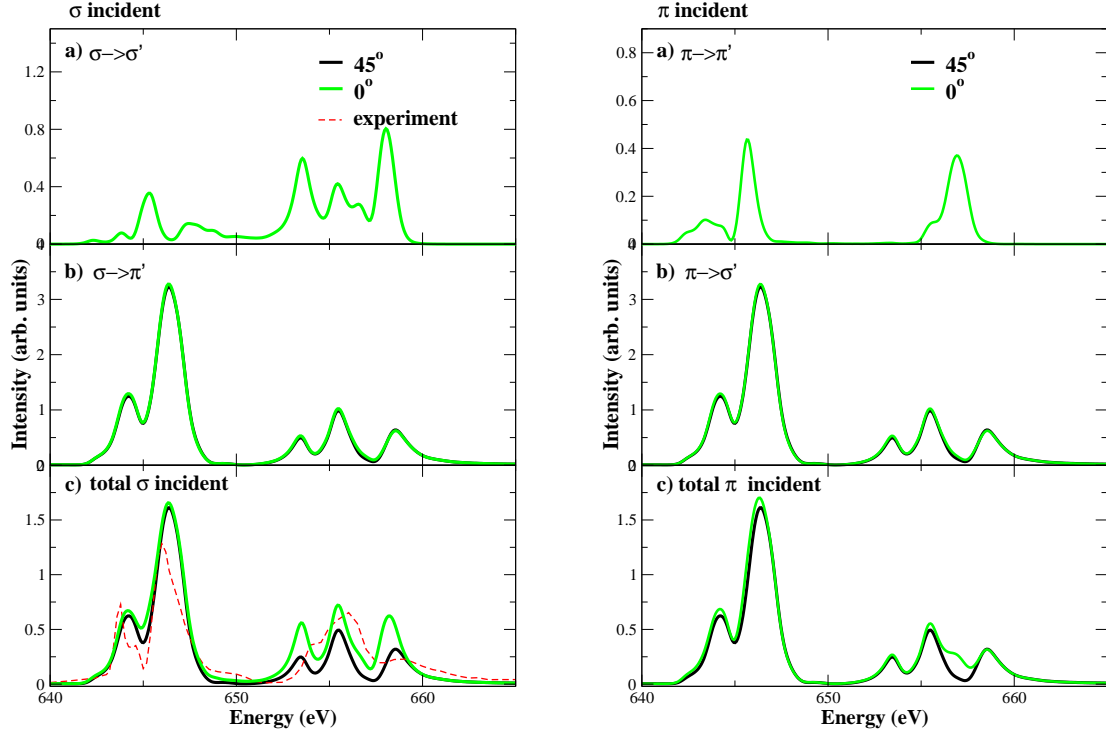


FIG. 4: Theoretical orbital order spectra of the CE structures with the two different spin orientations  $\alpha = 45^\circ$  (black line) and  $0^\circ$  (green line) calculated for  $\sigma$  and  $\pi$  incident polarizations. Different panels represent the polarization channels: for the  $\sigma$  incident a)  $\sigma \rightarrow \sigma'$ , b)  $\sigma \rightarrow \pi'$  and c) total, and for the  $\pi$  incident a)  $\pi \rightarrow \pi'$ , b)  $\pi \rightarrow \sigma'$  and c) total. The experimental spectrum (dashed red line) for  $\sigma$  incident polarization is reproduced from Ref. 11.

resolution.

The most significant difference between the spectra for the two angles  $\alpha$  are the nonvanishing  $\sigma \rightarrow \sigma'$  and  $\pi \rightarrow \pi'$  contributions for the  $0^\circ$  alignment. For this angle and in the case of the  $\sigma$  incident polarization, the scattering for the photon energies of the  $L_3$  edge is very small compared to the scattering at the  $L_2$  edge. For the  $\sigma \rightarrow \pi'$  polarization, the spectra for  $0^\circ$  and  $45^\circ$  alignments are identical, both in shape and magnitude. Similarly, for the  $\pi$  incident polarization, the  $\pi \rightarrow \pi'$  contribution is much smaller than for the  $\pi \rightarrow \sigma'$  scattering channel, the spectrum of which is again identical to the one obtained for  $\alpha = 45^\circ$ . This can be explained by considering a linear expansion of  $F^{A(B)}$  around the angle  $\alpha = 45^\circ$ . It can be shown (the details are given in Appendix B) that the first order corrections of four different  $F$  terms in Eq. 7 cancel exactly in the case of collinear spins, *i.e.* when the angle  $\alpha_A$  at the site A can be expressed as  $\alpha_A = 90^\circ - \alpha_B$ , leaving just the zeroth order

term which equals the scattering amplitude in the case of  $45^\circ$ . In the situation where both polarization channels contribute with the same weight, panel c), for the  $\sigma$  polarized incident light, the  $0^\circ$  spectrum has smaller  $L_3/L_2$  ratio because of the contribution from the  $\sigma \rightarrow \sigma'$  polarization which is significant only at the  $L_2$  edge. In the case of the  $\pi$  incident polarization, the branching ratio slightly increases for the unpolarized situation, as the  $\pi \rightarrow \pi'$  contribution at the  $L_3$  edge adds up to the main peak of the  $\pi \rightarrow \sigma'$  polarization, while the  $L_2$  contribution causes appearance of a new small feature in the unpolarized spectrum.

Considering only the situation c) (no outcoming polarization analysis), the orbital spectra calculated for the  $\alpha = 0^\circ$  and  $\alpha = 45^\circ$  structures show similar agreement with the experimental spectrum in Fig. 4c). In this situation, one cannot discriminate between the two cases. Very recently, however, experiments with a polarization analysis were performed on  $\text{La}_{0.5}\text{Sr}_{1.5}\text{MnO}_4$  (Ref. 9), and no detectable orbital scattering was observed for the  $\sigma \rightarrow \sigma'$  channel. Based on this observation, we conclude that the spin orientation in  $\text{La}_{0.5}\text{Sr}_{1.5}\text{MnO}_4$  should correspond to an angle  $\alpha$  equal to, or very close to, the value of  $45^\circ$ , since a measurable  $\sigma \rightarrow \sigma'$  component<sup>32</sup> should be present otherwise (see also Appendix A).

The magnetic spectra for the two CE structures are compared in Fig. 5. The main difference between the  $\alpha = 0^\circ$  and  $\alpha = 45^\circ$  cases is the decrease of the  $L_3/L_2$  branching ratio in the case  $\alpha = 0^\circ$ . Otherwise, the spectra have a similar shape. We note that  $\alpha = 45^\circ$  is also the value which was used in Ref. 11 to examine the effect of the Jahn-Teller distortion on the orbital and magnetic spectra of  $\text{La}_{0.5}\text{Sr}_{1.5}\text{MnO}_4$ . The experimental orbital and magnetic scattering spectra and fits for  $\text{La}_{0.5}\text{Sr}_{1.5}\text{MnO}_4$  have been presented and discussed in Ref. 11.

Our finding that  $\alpha \approx 45^\circ$  differs from the estimate of Staub *et al.*<sup>9</sup>, who predicted  $\alpha = 10 \pm 5^\circ$ , based on a fit focused on the contribution of minority ferromagnetic domains to the observed orbital scattering. We note, however, that the angle  $\alpha$  in the minority ferromagnetic domains and in the majority CE domains may not be necessarily the same.

To illustrate further the importance of taking into account the proper spin arrangement (and all four different scattering sites), we calculated the orbital scattering from the canted spin structures, in Fig. 2. The orbital spectra for the two canted structures are displayed in Fig. 6. It is clear that these two configurations yield spectra largely different from the experimental and theoretical spectra for  $\alpha = 45^\circ$ , and that the calculation of the orbital scattering in  $\text{La}_{0.5}\text{Sr}_{1.5}\text{MnO}_4$ , as shown in Fig. 4, should not be approximated by the consideration of

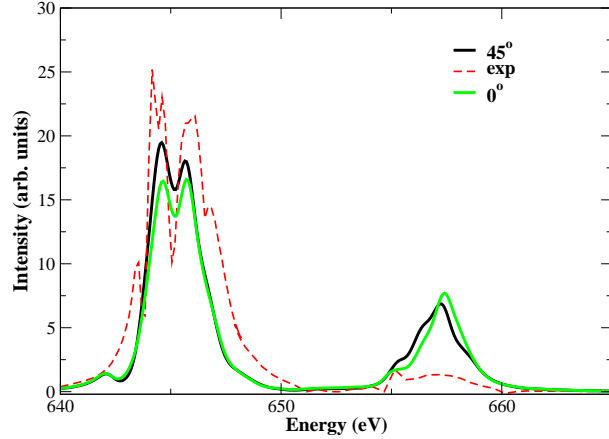


FIG. 5: Theoretical magnetic order spectra of the CE structures with the two different angles enclosed by the spin and  $\vec{b}$  axes ( $\alpha = 45^\circ$  and  $0^\circ$ ). The experimental spectrum (dashed red line) is reproduced from Ref. 11.

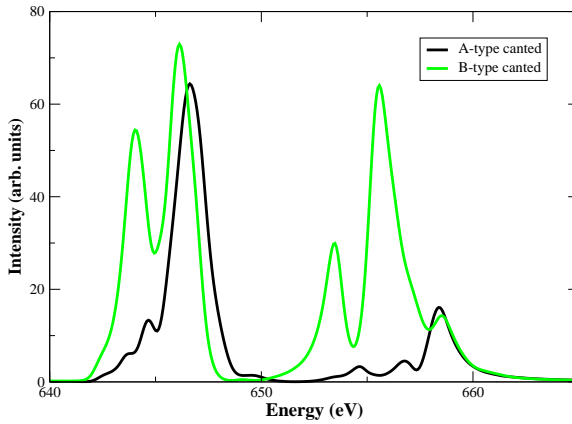


FIG. 6: Theoretical spectra of the orbital scattering for the A-type (black) and B-type (green)  $90^\circ$ -spin-canted structures, displayed in Fig. 2.

only one site of high symmetry, A or B. At the same time, even from a quick inspection of Fig. 6, one readily concludes that the two spectra are significantly different from each other. Yet, the only difference in their calculation was the spin arrangement. From this, we conclude that changing the spin arrangement can have a drastic influence on the orbital

spectrum. This must be related, of course, in some way to the spin-orbit interaction. To better identify the origin of this effect, we performed calculations with either (i) the  $d$  spin-orbit parameter set to zero or (ii) the  $p$ - $d$  interaction set to zero. Calculations (i) yielded only minute changes to the spectra. Calculations (ii), instead, yielded major changes, resulting in two virtually identical spectra for the A and B canted structures. Therefore, we conclude that the sensitivity to the spin direction comes from the combined effect of the spin-orbit interaction in the  $p$ -shell and the  $p$ - $d$  Coulomb interaction, through which  $p$ -electrons feel the crystal field.

## V. EFFECT OF DIFFERENT TYPES OF SPIN MISORIENTATIONS ON THE ORBITAL SPECTRUM IN THE PARAMAGNETIC PHASE

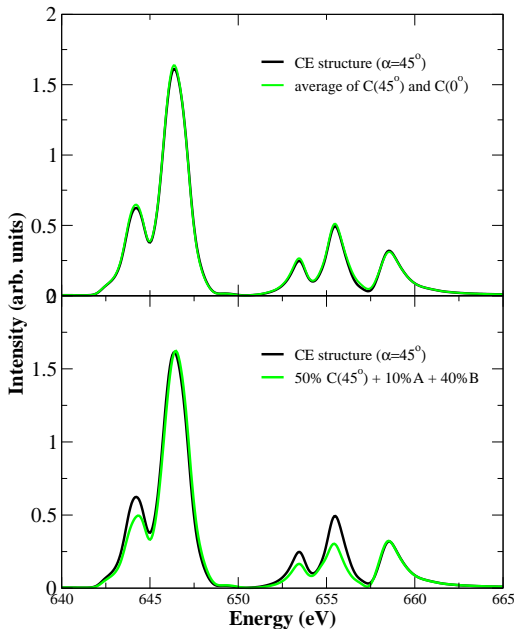


FIG. 7: Comparison of the theoretical orbital scattering spectra for  $\alpha = 45^\circ$  (black), and for configurations with different types of spin misorientations in the paramagnetic case (green), described in the text.

With the increase of temperature  $T$  above  $T_N$ , spin ordering is first lost along the c-axis, while the in-plane correlations reduce gradually until the charge and orbital ordering temperature  $T_{CO} = 230$  K, at which they vanish completely<sup>18</sup>. Based on the results from

the previous sections, we discuss the influence of various spin misorientations on the orbital spectrum in the paramagnetic phase for temperatures  $T_N \leq T \ll T_{CO}$ , when there are still correlations inside the  $ab$ -plane. Randomness is expected to be mostly in the spin orientation between the planes, while the antiferromagnetic ordering inside the planes is assumed to be less influenced. We calculate the scattering contributions at  $\vec{q} = (\frac{1}{4}, \frac{1}{4}, 0)$  from CE  $ab$ -planes with different spin orientations for the angles belonging to the class of  $\alpha = 45^\circ + n \times 90^\circ$  ( $n$  integer), which we defined as  $C(45^\circ)$ , and the class of  $\alpha = 0^\circ + n \times 90^\circ$ ,  $C(0^\circ)$ , *i.e.* for  $\alpha = 0^\circ, 45^\circ, 90^\circ, 135^\circ, 180^\circ, 225^\circ, 270^\circ$  and  $315^\circ$ . These planes are stacked in a random order, but assuming an equal proportion of each of them. In this case, the scattering amplitude is given by the average of the scattering amplitudes of the  $\alpha = 45^\circ, 135^\circ, 0^\circ$ , and  $90^\circ$  cases. The corresponding orbital spectrum is shown in panel a) of Fig. 7 for the incident  $\sigma$  polarization. We see that the spectrum does not change with respect to the spectrum obtained for the CE phase ( $\alpha = 45^\circ$ ). This is because the  $\sigma \rightarrow \pi'$  scattering amplitudes for  $\alpha = 0^\circ, 45^\circ, 90^\circ$ , and  $135^\circ$  are all equal, and with an equal amount of  $\alpha = 0^\circ$  and  $\alpha = 90^\circ$  layers, the atomic scattering amplitude for the  $\sigma \rightarrow \sigma'$  scattering component vanishes, reducing the spectrum to the  $\sigma \rightarrow \pi'$  scattering component. Furthermore, assuming also a loss of coherence in the spin orientation between ferromagnetic chains within the  $ab$ -plane and a random occurrence of the angles belonging to the classes  $C(45^\circ)$  and  $C(0^\circ)$  for the ferromagnetic chains, the scattering amplitude can also be shown to be that corresponding to the average of the  $\alpha = 0^\circ, \alpha = 90^\circ$ , and  $\alpha = 45^\circ$  amplitudes.

Hence, to produce a significant change in the orbital scattering, it is necessary to consider other changes (with a higher degree of misorientation) in the spin configurations, such as canted “ferromagnetic” chains. We find, however, that an equal amount of A and B-type canted configurations yields a spectrum identical to the one for the CE phase, and that it is necessary to consider a different amount of the two canted structures to change the spectrum. The orbital scattering spectrum for the case when 50 % of the sites corresponds to the configurations described with  $C(45^\circ)$ , 10 % to the A-type canted and 40 % to the B-type canted configurations is shown in b) panel of Fig. 7. The spectrum is characterized by the reduction of intensity of the first two peaks at the  $L_2$  edge, as well as of the low-energy peak at the  $L_3$  edge. The experimental data of Wilkins *et al.*<sup>10</sup> indicate a large change of intensity at the  $L_3$  peak, a weaker one for the two low-energy peaks at the  $L_2$  edge, and virtually no change for the high-energy  $L_2$  peak. A qualitatively similar trend

can be deduced from comparing the orbital spectra at 40 K and 160 K, measured by Staub *et al.*<sup>9</sup>, for which the largest intensity reduction occurs at the L<sub>3</sub> edge and the low-energy peaks at the L<sub>2</sub> edge, while the intensity of the highest-energy feature changes much less. A large change in the intensity of the main peak at the L<sub>3</sub> edge of the orbital spectrum at the Néel temperature could result from the magnetic scattering of the minority ferromagnetic domains, which would disappear above  $\sim T_N$ <sup>9</sup>. A similar effect, *i.e.* a significant reduction of the main peak at the L<sub>3</sub> edge and almost negligible changes of the other peaks, could also result from a decrease in the Jahn-Teller distortion<sup>11</sup>. However, the change in intensity of the other peaks is difficult to explain with the above effects, and Fig. 7b indicates that they could be accounted for by a change in the spin configuration.

## VI. CONCLUSIONS

In this work, we analyzed the dependence of the scattering spectra on the spin configuration in La<sub>0.5</sub>Sr<sub>1.5</sub>MnO<sub>4</sub>. We considered an arbitrary spin direction with respect to the local crystal field axis, yielding a low local symmetry, which necessitated a general scattering formula written for the C<sub>i</sub> point group. We generalized the Hannon-Trammel formula for the atomic scattering amplitude by a systematic expansion in invariants of decreasing symmetry up to C<sub>i</sub> and implemented it in the framework of atomic multiplet calculations in a crystal field. We discussed in detail the cases of four different spin structures.

We first considered two antiferromagnetic CE structures with spins oriented either along the  $\vec{b}$  axis or along an axis at an angle  $\alpha = 45^\circ$  relative to the  $\vec{b}$  axis, within the *ab*-plane. The latter structure has the highest symmetry (all sites are related by symmetry operations) and has only the  $\sigma \rightarrow \pi'$  orbital scattering for  $\sigma$  incident light which is confirmed by recent experiments which found no  $\sigma \rightarrow \sigma'$  scattering component. For the consideration of the CE structure with spins aligned with the lattice vector  $\vec{b}$  ( $\alpha = 0^\circ$ ), one needs to include an equal amount of sites which have spins either at  $0^\circ$  or at  $90^\circ$  with respect to the local crystal field axis in order to keep a collinear spin configuration. Orbital scattering in the  $\sigma \rightarrow \pi'$  channel for the cases  $\alpha = 45^\circ$  and  $\alpha = 0^\circ$  yields identical spectra, but in the latter case the scattering also takes place in the  $\sigma \rightarrow \pi'$  channel, in contrast to the experimental situation. Similarly, for the incident  $\pi$  polarization, there is a nonvanishing  $\pi \rightarrow \pi'$  contribution, and the spectrum of the  $\pi \rightarrow \sigma'$  channel is identical to the one for  $\alpha = 45^\circ$ . For the magnetic

scattering, the spectrum of the configuration with  $\alpha = 45^\circ$  displays a somewhat larger  $L_2/L_3$ . From the comparison with experiment, we conclude that in the  $\text{La}_{0.5}\text{Sr}_{1.5}\text{MnO}_4$  CE phase the angle between the spins and  $\vec{b}$  axis is equal, or very close to,  $45^\circ$ .

We then also examined two  $90^\circ$ -spin-canted structures obtained by considering only sites having the spin direction either at  $0^\circ$  or at  $90^\circ$  from the local crystal field axis. The spectra differ greatly in the two cases, and also differ from those obtained for the antiferromagnetic CE structures. From the consideration of these structures, we thus conclude that the spin configuration can have a drastic influence on the orbital spectrum.

Finally, we also discussed the changes observed with temperature, in the orbital spectrum of the paramagnetic phase, considering the effect of various types of spin misorientations with respect to the CE structure. We first examined the effect of an incoherence in the spin orientation between the  $ab$ -planes and then also between the ferromagnetic chains within the  $ab$ -planes, considering ferromagnetic chains with spin directions corresponding to  $\alpha = 0^\circ, 45^\circ, 90^\circ, 135^\circ, 180^\circ, 225^\circ, 270^\circ$ , and  $315^\circ$ . This was found to have a negligible effect on the orbital spectrum. We then examined the effect of an incoherence in the spin direction within the ferromagnetic chains, considering the contributions of different types of  $90^\circ$ -spin-canted chains. This resulted in a spectrum with no change in the highest-energy peak, both at the  $L_2$  and  $L_3$  edges, and a reduced intensity of all the other peaks. In the view of the measured temperature dependence of the orbital scattering intensity, the changes of the spectrum caused by the spin misorientations can complement the effects which would arise due to the presence of possible minority ferromagnetic domains or a reduction in the Jahn-Teller distortion, which would mostly affect the highest-energy peak at the  $L_3$  edge.

#### **APPENDIX A: ORBITAL AND MAGNETIC SCATTERING FOR AN ARBITRARY ANGLE BETWEEN THE SPIN AND LATTICE AXES**

Previously, we discussed the scattering in the CE structure when the in-plane spin and lattice axes enclose angles of  $0^\circ$  or  $45^\circ$ . At this point, we present the expression for the orbital scattering amplitude in the case of an arbitrary angle  $\alpha$  between the spin axis and

lattice vector  $\vec{b}$  for  $\sigma$ -polarized incident light:

$$f_{\text{res}}^{\text{OO},\sigma\text{inc}} = \left\{ \begin{array}{l} \sin^2 \beta \cos^2 \phi \\ \frac{1}{2}(\sin^2 \beta \sin \theta \sin 2\phi - \sin 2\beta \cos \theta \cos \phi) \\ \cos^2 \beta \cos^2 \phi + \sin^2 \phi \\ \frac{1}{2}[\sin 2\phi \sin \theta(1 - \cos^2 \beta) + \sin 2\beta \cos \theta] \\ \cos^2 \beta \cos^2 \phi - \sin^2 \phi \\ \frac{1}{2}[\sin 2\phi \sin \theta(\cos^2 \beta + 1) + \sin 2\beta \cos \theta] \\ \frac{1}{2} \sin 2\beta \cos^2 \phi \\ \frac{1}{2} \sin 2\beta \sin \theta \sin 2\phi + \cos 2\beta \cos \theta \cos \phi \end{array} \right\} \left\{ \begin{array}{l} 2(F_{0;0}^{A+} - F_{0;0}^{B+}) + \\ (F_{-1;-1}^{A+} + F_{1;1}^{A+} - F_{-1;-1}^{B+} - F_{1;1}^{B+}) + \\ (F_{-1;1}^{A+} + F_{1;-1}^{A+} - F_{-1;1}^{B+} - F_{1;-1}^{B+}) \\ (F_{1;0}^{A+} + F_{0;-1}^{A+} - F_{-1;0}^{A+} - F_{0;1}^{A+} - \\ F_{1;0}^{B+} - F_{0;-1}^{B+} + F_{-1;0}^{B+} + F_{0;1}^{B+}) \end{array} \right\} \quad (A1)$$

where we used  $\beta = \alpha - 45^\circ$  and the definitions of  $\theta$  and  $\phi$  from Fig 3. We remind the reader that the  $F_{m,m'}$  spherical tensor components are defined with respect to the spin axis, and that their values change with the angle  $\alpha$ . We also note that there is an additional term in the scattering amplitude (the last term in the above equation), with respect to Eq. 6, which does not vanish in the general case. In Cartesian coordinates this term is proportional to  $F_{xz} + F_{zx}$ . Considering, *e.g.*, the azimuthal angle  $\phi = 0^\circ$ , we note that there is a  $\sigma \rightarrow \sigma'$  scattering component for all angles  $0 \leq \alpha \leq 90^\circ$ , except for  $\alpha = 45^\circ$ .

In the case of magnetic scattering, there are no additional terms (compared to Eqs. 10 and 11) contributing to the scattering. The scattering always takes place only in the  $\sigma \rightarrow \pi'$  channel.

## APPENDIX B: LINEAR EXPANSION OF $F_{m,m'}$ AROUND $\alpha_{A(B)} = 45^\circ$

If we denote the angle between the spin and the local crystal field axis at site A (B) as  $\alpha_A$  ( $\alpha_B$ ), then the two angles in Fig. 1, Case II, are related by:  $\alpha_A = 90^\circ - \alpha_B$ . We will expand the tensor  $F_{m,m'}^A$  defined in Eq. 2, as a function of the angle  $\alpha_A$  around  $45^\circ$  in the following way:

$$F_{m,m'}^A(\alpha_A) = F_{m,m'}^A(45^\circ) + \frac{\delta F_{m,m'}^A(\alpha_A)}{\delta \alpha_A} \Big|_{\alpha_A=45^\circ} (\alpha_A - 45^\circ) + O(\Delta \alpha_A^2). \quad (B1)$$

The same expansion is valid for  $F_{m,m'}^B$ . Therefore, for the  $F_{xx}^A$  and  $F_{zz}^B$  from Eq. 7, we can write:

$$F_{xx}^A(\alpha_A) = F_{xx}^A(45^\circ) + \frac{\delta F_{xx}^A(\alpha_A)}{\delta \alpha_A} \Big|_{\alpha_A=45^\circ} (\alpha_A - 45^\circ) + O(\Delta \alpha_A^2), \quad (B2)$$

where  $x$  is the coordinate along  $\vec{a}$  and  $z$  the coordinate along  $\vec{b}$ . We can also write:

$$\begin{aligned} F_{zz}^B(\alpha_B) &= F_{zz}^B(45^\circ) + \frac{\delta F_{zz}^B(\alpha_B)}{\delta \alpha_B} \Big|_{\alpha_B=45^\circ} (\alpha_B - 45^\circ) + O(\Delta \alpha_B^2) \\ &= F_{xx}^A(45^\circ) + \frac{\delta F_{xx}^A(\alpha_A)}{\delta \alpha_A} \Big|_{\alpha_A=45^\circ} (45^\circ - \alpha_A) + O(\Delta \alpha_A^2), \end{aligned} \quad (\text{B3})$$

using the fact that  $\Delta \alpha_A = -\Delta \alpha_B$  and that  $F_{xx}^A(45^\circ) = F_{zz}^B(45^\circ)$  and  $\frac{\delta F_{xx}^A(\alpha_A)}{\delta \alpha_A} \Big|_{\alpha_A=45^\circ} = \frac{\delta F_{zz}^B(\alpha_B)}{\delta \alpha_B} \Big|_{\alpha_B=45^\circ}$ , because the atomic scattering tensor  $F^A(\alpha_A = 45^\circ + \Delta \alpha_A)$  at the A site is equivalent to the atomic scattering tensor  $F^B(\alpha_B = 45^\circ + \Delta \alpha_A)$  at the B site through a rotation of  $180^\circ$  about the  $\vec{a} + \vec{b}$  axis. In the intensity expression, Eq. 7,  $F_{xx}^A$  and  $F_{zz}^B$  are added up. From Eqs. B2 and B3, we see that the two first order terms will have the same magnitude and opposite signs. The same can be shown for the remaining terms from Eq. 7,  $F_{zz}^A$  and  $F_{xx}^B$ , thus proving that the first order terms in the expression for the intensity all vanish, leaving only the zeroth order term equal to the  $45^\circ$  contribution. We also tested the assumption of a linear dependence of  $F_{m,m'}$  on the angle around  $45^\circ$  by checking numerically the linear-order result:

$$F_{xx}^A(\alpha_A = 0^\circ) + F_{xx}^A(\alpha_A = 90^\circ) = 2F_{xx}^A(\alpha = 45^\circ), \quad (\text{B4})$$

and confirmed that the dependence  $F_{m,m'}(\alpha)$  is described well (within the numerical noise) with the expansion up to the first order.

## ACKNOWLEDGMENTS

We are grateful to P. Carra for helpful discussions and his assistance in learning how to use the Cowan and “Racah” codes. We acknowledge stimulating discussions with G. Trimarchi.

---

<sup>1</sup> Y. Moritomo, A. Asamitsu, H. Kuwahara, and Y. Tokura, *Nature* **380**, 141 (1996).  
<sup>2</sup> J. B. Goodenough, *Phys. Rev.* **100**, 564 (1955).  
<sup>3</sup> I. S. Elfimov, V. I. Anisimov, and G. A. Sawatzky, *Phys. Rev. Lett.* **82**, 4264 (1999).  
<sup>4</sup> M. Benfatto, Y. Joly, and C. R. Natoli, *Phys. Rev. Lett.* **83**, 636 (1999).  
<sup>5</sup> P. Benedetti, J. van den Brink, E. Pavarini, A. Vigliante, and P. Wochner, *Phys. Rev. B* **63**, 060408 (2001).  
<sup>6</sup> S. B. Wilkins, P. D. Hatton, M. D. Roper, D. Prabhakaran, and A. T. Boothroyd, *Phys. Rev. Lett.* **90**, 187201 (2003).  
<sup>7</sup> S. S. Dhesi, A. Mirone, C. D. Nadai, P. Ohresser, P. Bencok, N. B. Brookes, P. Reutler, A. Revcolevschi, and A. Tagliaferri, *Phys. Rev. Lett.* **92**, 056403 (2004).

<sup>8</sup> K. J. Thomas, J. P. Hill, S. Grenier, Y.-J. Kim, P. Abbamonte, L. Venema, A. R. Y. Tomioka, Y. Tokura, D. F. McMorrow, G. Sawatzky, et al., Phys. Rev. Lett. **92**, 237204 (2004).

<sup>9</sup> U. Staub, V. Scagnoli, A. M. Mulders, K. Katsumata, Z. Honda, H. Grimmer, M. Horisberger, and J. M. Tonnerre, Phys. Rev. B **91**, 177201 (2005).

<sup>10</sup> S. B. Wilkins, P. D. Spencer, P. D. Hatton, S. P. Collins, M. D. Roper, D. Prabhakaran, and A. T. Boothroyd, Phys. Rev. Lett. **91**, 167205 (2003).

<sup>11</sup> S. B. Wilkins, N. Stojic, T. A. W. Beale, N. Binggeli, C. W. M. Castleton, P. Bencok, D. Prabhakaran, A. T. Boothroyd, P. D. Hatton, and M. Altarelli (2005), submitted to Phys. Rev. B, cond-mat/0410713.

<sup>12</sup> C. W. M. Castleton and M. Altarelli, Phys. Rev. B **62**, 1033 (2000).

<sup>13</sup> Y. Murakami, J. P. Hill, D. Gibbs, M. Blume, I. Koyama, M. Tanaka, H. Kawata, T. Arima, Y. Tokura, K. Hirota, et al., Phys. Rev. Lett. **81**, 582 (1998).

<sup>14</sup> L. Paolasini, R. Caciuffo, A. Sollier, P. Ghigna, and M. Altarelli, Phys. Rev. Lett. **88**, 106403 (2002).

<sup>15</sup> R. Caciuffo, L. Paolasini, A. Sollier, P. Ghigna, E. Pavarini, J. van den Brink, and M. Altarelli, Phys. Rev. B. **65**, 174425 (2002).

<sup>16</sup> J. P. Hannon, G. T. Trammell, M. Blume, and D. Gibbs, Phys. Rev. Lett. **61**, 1245 (1988).

<sup>17</sup> S. Larochelle, A. Mehta, L. Lu, P. K. Mang, O. P. Vajk, N. Kaneko, J. W. Lynn, L. Zhou, and M. Greven, Phys. Rev. B **71**, 024435 (2005).

<sup>18</sup> B. J. Sternlieb, J. P. Hill, U. C. Wildgruber, G. M. Luke, B. Nachumi, Y. Moritomo, and Y. Tokura, Phys. Rev. Lett. **76**, 2169 (1996).

<sup>19</sup> J. Herrero-Martin, J. Garcia, G. Subias, J. Blasco, and M. C. Sánchez, Phys. Rev. B **70**, 024408 (2004).

<sup>20</sup> There is experimental indication for the spin direction in the [210]-direction<sup>18</sup>. However, in the present study, we will consider two different spin orientations and, on the basis of theoretical considerations and indirect experimental evidence, propose the alternative spin arrangement.

<sup>21</sup> G. van der Laan and B. T. Thole, Phys. Rev. B **43**, 13401 (1991).

<sup>22</sup> F. de Groot, Coordin. Chem. Rev. **249**, 31 (2005).

<sup>23</sup> R. D. Cowan, J. Opt. Soc. Am. **58**, 808 (1968).

<sup>24</sup> R. D. Cowan, *The Theory of Atomic Structure and Spectra* (University of California Press, Berkeley, 1981).

<sup>25</sup> F. M. F. de Groot, J. C. Fuggle, B. T. Thole, and G. A. Sawatzky, Phys. Rev. B **42**, 5459 (1990).

<sup>26</sup> A. Thomson, D. Vaughan, E. Gullikson, M. Howells, K.-J. Kim, J. Kirz, J. Kortright, I. Lindau, P. Pianetta, A. Robinson, et al., *X-Ray Data Booklet* (Lawrence Berkeley National Laboratory, University of California, Berkeley, CA 94720, 2001).

<sup>27</sup> P. H. Butler, *Point Group Symmetry Applications* (Plenum Press, New York, 1981).

<sup>28</sup> M. Abbate, F. M. F. de Groot, J. C. Fuggle, A. Fujimori, O. Strelbel, F. Lopez, M. Domke, G. Kaindl, G. A. Sawatzky, M. Takano, et al., Phys. Rev. B **46**, 4511 (1992).

<sup>29</sup> Larochelle *et al.*<sup>17</sup> find a small orthorhombic field ( $C_{2h}$ -point group). We approximate it by the tetragonal field, as our calculations including the orthorhombic contributions to the crystal field<sup>11</sup> did not show any significant changes with respect to the crystal field of the  $C_{4h}$  symmetry.

<sup>30</sup> P. Carra and B. T. Thole, Rev. of Mod. Phys. **66**, 1509 (1994).

<sup>31</sup> The matrix elements from Eq. 2 are evaluated for the spherical symmetry case, yielding either a finite real or zero value. By repeated application of the Wigner-Eckart theorem (multiplication with the corresponding 2-j and 3-j coefficient) these matrix elements are “lowered” to the final

symmetry. All 2-j and 3-j coefficients in the applied symmetry branching are real and, therefore, the final matrix elements and  $F$ 's itself are real.

<sup>32</sup> The atomic scattering amplitudes of the configurations with  $\alpha = 0^\circ$  and  $\alpha = 90^\circ$  are the same for the  $\sigma \rightarrow \pi'$ , and of opposite sign for the  $\sigma \rightarrow \sigma'$  scattering channel. The coexistence of both configurations in domain structures might lead to the conclusion that also in this case the  $\sigma \rightarrow \sigma'$  scattering component vanishes. However, we note that considering also the domains corresponding to the two equivalent  $A - B - A - B - \dots$  and  $B - A - B - A - \dots$  arrangements of orbitally ordered planes, which have, in principle, identical probability to occur, the  $\alpha = 0^\circ$  and  $\alpha = 90^\circ$  domains are expected to give contributions to the scattering amplitude which are out of phase with each other. Their signals, therefore, should be added on the level of intensity, thus keeping the same proportion of the  $\sigma \rightarrow \sigma'$  scattering component in the total signal.